PHOTONICS Research

Inorganic lead-free cesium copper chlorine nanocrystal for highly efficient and stable warm white light-emitting diodes

Shuangyi Zhao,† Qionghua Mo,† Wensi Cai, Huaxin Wang, and Zhigang Zang*

Key Laboratory of Optoelectronic Technology & Systems (Ministry of Education), Chongqing University, Chongqing 400044, China
**Corresponding author: zangzg@cqu.edu.cn*

Received 3 September 2020; revised 27 October 2020; accepted 7 December 2020; posted 15 December 2020 (Doc. ID 409398); published 26 January 2021

Inorganic cesium lead halide ($CsPbX_3$, X = Cl, Br, I) nanocrystals (NCs) attract extensive attention because of their excellent optoelectronic performance. However, the classic $CsPbX_3$ NCs suffer from toxicity and instability, which impede their further applications in commercial fields. Here the inorganic lead-free cesium copper chlorine NCs are synthesized by a facile hot-injection method. The blue-emission 3D $CsCu_2Cl_3$ and green-emission 0D $Cs_3Cu_2Cl_5$ NCs are prepared at 70°C and 120°C, respectively, suggesting that the reaction temperature may account for the final components. Owing to the self-trapped exciton effect, the unique optical properties, such as high photoluminescence (PL) quantum yield, broadband emission, large Stokes shift, and long PL decay time, are demonstrated for both cesium copper chlorine NCs. Moreover, highly efficient and stable warm white light-emitting diodes are fabricated with $CsCu_2Cl_3$ and $Cs_3Cu_2Cl_5$ NCs. The study highlights the promising potential for lead-free cesium copper chlorine nanocrystals in nontoxic solid-state lighting applications.

https://doi.org/10.1364/PRJ.409398

1. INTRODUCTION

Owing to the high photoluminescence quantum yield (PLQY), near-narrow bandwidth, high absorption coefficient, and tunable emission covering the entire visible spectral region [1–4], inorganic cesium lead halide ($CsPbX_3$, X = Cl, Br, I) perovskite nanocrystals (NCs) have exhibited excellent performance in optoelectronic devices, including light-emitting diodes (LEDs) [5,6], solar cells [7–10], and photodetectors [11]. However, the toxicity of the lead (Pb) element in the $CsPbX_3$ NCs may impede their commercial applications. To address this serious issue, the doping of nontoxic elements and synthesis of inorganic lead-free perovskite have been proposed [12,13]. Nontoxic elements, including tin (Sn) [14], antimony (Sb) [15], bismuth (Bi) [16], indium (In) [17], silver (Ag) [18], and copper (Cu) [19–21], were previously reported to replace lead to form 0D and double perovskite NCs. However, due to the strong reducibility and high defect density, the reported lead-free $CsSnX_3$, $Cs_3Bi_2X_9$, and Cs_2AgInX_6 NCs (X = Cl, Br, I) had low PLQY and instability, which have become critical issues for commercial applications [15,16,22].

Therefore, among the low-dimension lead-free nanocrystals, cesium copper (Cu) halide is one of the attractive materials, which is due to its abundance, low cost, and nontoxicity [23–25]. In addition, owing to the three- or fourfold coordination for Cu $3d^{10}$ orbitals and the small radius of the monovalent Cu^+ ions, monovalent Cu^+ ions tend to be surrounded by three and four halide ions, forming $[CuX_3]$ triangles and $[CuX_4]$ tetrahedra (X = halogen), respectively [26]. The DFT (density functional theory) calculation results demonstrated that the Cu $3d^{10}$ orbitals could hybridize with halogen p orbitals to lower the energy of orbitals, leading to the spatial spread of the relevant atomic orbitals [27]. Compared with the $[PbX_6]$ octahedron, the $[CuX_3]$ triangles and $[CuX_4]$ tetrahedra showed higher exciton binding energy. Therefore, researchers have paid more attention to the low-dimension cesium copper (monovalence) halide, including $CsCu_2I_3$ [28], $Cs_3Cu_2Br_{5-x}I_x$ [29], $CsCuBr_2$ [30], and Cs_2CuBr_4 [31]. Among them, the $Cs_3Cu_2I_5$ and $Cs_3Cu_2Br_5$ synthesized by the hot-injection method exhibited bright-blue emission with PLQY as high as 67% and 18.3%, respectively [32,33]. However, the cesium copper (monovalence) chlorine NCs have not been investigated clearly up to now. Besides, it is quite urgent to further research the reaction temperature of the hot-injection method, as it plays a critical role in the components of the cesium copper (monovalence) chlorine colloidal perovskite.

In this study, we reported the synthesis of cesium copper (monovalence) chlorine NCs, and the results demonstrated that the components could be decided from the reaction temperature. The 3D $CsCu_2Cl_3$ and 0D $Cs_3Cu_2Cl_5$ NCs were synthesized at 70°C and 120°C, respectively. The 3D $CsCu_2Cl_3$ exhibited a blue emission with a PLQY of 47.8%, while the 0D

$Cs_3Cu_2Cl_5$ NCs showed a bright-green emission with a PLQY as high as 84.2%. In addition, the results revealed that the large Stokes shifts with broadband emission existed in both cesium copper chlorine NCs, which might arise from the strong quantum confinement and the self-trapped exciton (STE) effect. The Jahn–Teller distortion of the $[CuCl_3]$ triangle and $[CuCl_4]$ tetrahedron enabled excitons to be localized and emitted strongly, accounting for the excellent optical performance of cesium copper chlorine nanocrystals. Furthermore, the $CsCu_2Cl_3$ and $Cs_3Cu_2Cl_5$ NCs with strong blue and green photoluminescence (PL) were used to prepare the warm white light-emitting diodes (WLEDs). The obtained WLEDs, which consisted of nontoxic $Cs_3Cu_2Cl_5$ NCs, $CsCu_2Cl_3$ NCs, and red phosphors, exhibited a high color rendering index (CRI) of 94 and an appropriate correlated color temperature (CCT) of 5285 K. Moreover, the WLEDs showed an excellent operating stability with the luminous efficiency (LE) maintaining 64% of its initial value, even after 60 h. The high CRI (>92) was also sustained after continuous operation in air (30°C and 50% RH) for 60 h. This may suggest that inorganic cesium copper chlorine nanocrystals might have great potentials in next-generation nontoxic solid-state illuminating systems.

2. EXPERIMENT

Materials. Cesium carbonate (Cs_2CO_3, 99.9%) and copper (monovalence) chloride (CuCl, 99.9%) were purchased from Xi'an Polymer Light Technology Corp. Oleic acid (OA, >90%), oleylamine (OAm, >90%), and octadecene (ODE, >90%) were purchased from Adamas. Polymethyl methacrylate (PMMA) was purchased from Sigma Corp. All these reagents were used without further purification.

Synthesis of $Cs_3Cu_2Cl_5$ and $CsCu_2Cl_3$. 305 mg Cs_2CO_3, 15 mL ODE, and 1 mL OA were loaded into a 100 mL three-neck flask to prepare the Cs precursor. 39.6 mg CuCl and 10 mL ODE were loaded into another 100 mL three-neck flask. The two flasks were first degassed for 15 min. Then the flasks were heated to 120°C, and then 0.5 mL OAm and 0.5 mL OA were quickly injected into the Cu flask at 120°C under nitrogen flow. After 10 min, the temperature was changed/remained at 70/120°C. After remaining at the corresponding temperature for 2 min, 3 mL Cs precursor was quickly injected into the Cu flask, and the mixture was cooled in an ice-water bath to room temperature after 30 s.

Fabrication of the WLED. The 5 mL as-synthesized copper halide perovskite was centrifuged for 5 min at 10,000 r/min, and the supernatant was discarded. The pellet was resuspended in the toluene. The red $CaAlSiN_3:Eu^{2+}$ phosphors were added into the equal amounts of transparent epoxy A and B to mix together, and then they were coated on a 290 nm commercial UV chip. The chip with red phosphors was heated in an oven at 90°C for 1 h for solidification. The $Cs_3Cu_2Cl_5$ and $Cs_3Cu_2I_5$ powder with optimum amount was added into a PMMA/toluene solution. The blend was stirred for 30 min and then coated on the top of the chip. Finally, the WLED was heated on a hot plate at 50°C for 10 min to remove the solvent.

Characterizations. The crystal phases of the samples were characterized by X-ray diffraction (XRD) with Cu Kα radiation (XRD-6100, Shimadzu, Japan). The transmission electron microscopy (TEM) image was measured by an electron microscope (Libra 200 FE, Zeiss, Germany). The absorption spectrum was recorded ranging from 300 to 800 nm by a UV–vis spectrophotometer (UV-3800, Shimadzu, Japan) under room temperature. The PL spectroscopy data was measured by a fluorescence spectrophotometer (Agilent Cary Eclipse, Australia). The X-ray photoelectron spectroscopy (XPS) characterization was performed on an Escalab 250 Xi. PL spectroscopy and the data of PLQY were measured by a PL system. A PL system (FLS920, Edinburgh Instruments) that was capable of measuring PL and PLQYs with an integration sphere was employed in this work. Optical properties (CCT, CRI, and CIE color coordinates) of the WLED were measured using a spectroradiometer system (PR670, Photo Research).

3. RESULTS AND DISCUSSION

The synthesis of the cesium copper chlorine colloidal perovskite was described in Section 2. The XRD patterns shown below illustrate that the cesium copper chlorine colloidal perovskite synthesized at 70°C and 120°C is indexed as $CsCu_2Cl_3$ and $Cs_3Cu_2Cl_5$, respectively. While cesium lead halide ($CsPbX_3$, X = Cl, Br, I) perovskites show the cubic phase, orthorhombic phases are found for both $CsCu_2Cl_3$ and $Cs_3Cu_2Cl_5$ [29]. Some impure peaks are found in the XRD pattern of $CsCu_2Cl_3$, which are indexed as the phase of Cs_2CuCl_4 and might be due to the oxidation of the $CsCu_2Cl_3$. In contrast, the phase pattern of the Cs_2CuCl_4 is not found in the $Cs_3Cu_2Cl_5$ XRD results, implying the good stability of $Cs_3Cu_2Cl_5$ in the ambient condition. The morphology of the cesium copper chlorine nanocrystals synthesized by the hot-injection method is sensitive to the reaction temperature. To study this, TEM characterization was carried out for $Cs_3Cu_2Cl_5$ and $CsCu_2Cl_3$ with the representative results shown in Fig. 1. Figure 1(a) shows the TEM image of 0D $Cs_3Cu_2Cl_5$ NCs,

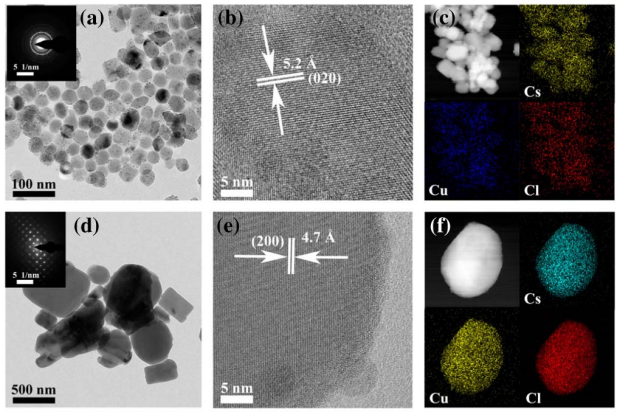

Fig. 1. (a) Transmission electron microscopy (TEM), (b) high-resolution TEM (HRTEM) images, and (c) corresponding cesium (Cs), copper (Cu), and chlorine (Cl) elemental mapping images of $Cs_3Cu_2Cl_5$ NCs. The inset shows selected-area electron diffraction images. (d) TEM, (e) HRTEM images, and (f) Cs, Cu, and Cl elemental mapping of $CsCu_2Cl_3$ NCs, respectively. The inset is the corresponding selected-area electron diffraction image.

which have polygon morphology with the average size of 35 nm.

Their crystallinity is evidenced by the selected-area electron diffraction image [the inset of Fig. 1(a)]. An interplanar distance of 5.2 Å (1 Å = 0.1 nm) corresponds to a (020) plane of $Cs_3Cu_2Cl_5$ NCs [Fig. 1(b)]. In contrast, the TEM results exhibit the irregular-shaped $CsCu_2Cl_3$ NCs with the size of hundreds of nanometers as shown in Fig. 1(d). The increase of size to hundreds of nanometers may be attributed to the intrinsic 3D structure and the aggregation of the $CsCu_2Cl_3$. The clear lattice fringes also demonstrate their excellent 3D crystallinity, as shown in Fig. 1(e), in which the (200) planes with interplanar distance of 4.7 Å can be found. Please note that the dimensions mentioned above are both morphological, which is consistent with the size of $Cs_3Cu_2Cl_5$ and $CsCu_2Cl_3$. In addition, the elemental mapping characterization of the 0D $Cs_3Cu_2Cl_5$ and 3D $CsCu_2Cl_3$ NCs was performed to confirm the presence of Cs, Cu, and Cl, as shown in Figs. 1(c) and 1(f), respectively. The elemental mapping results demonstrate the homogeneous distribution of the three elements in both samples, suggesting uniform components and pure phases.

The high-resolution XPS spectrum [Fig. 2(b)] shows the presence of monovalent Cu^+ (932.0 and 954.2 eV) with two satellite peaks at 934.4 and 962.3 eV attributing to divalent Cu^{2+}. The presence of Cu^{2+} might be due to the oxidation of Cu^+ [34]. The Cs and Cl XPS spectra of $CsCu_2Cl_3$ and $Cs_3Cu_2Cl_5$ are displayed in Figs. 2(c) and 2(d), respectively. The small shift in the XPS peaks of the Cl element between $CsCu_2Cl_3$ and $Cs_3Cu_2Cl_5$ NCs might be derived from the difference of the sites of Cl atoms. Specifically, the basic structure of $CsCu_2Cl_3$ is expected to be a $[CuCl_4]$ tetrahedron, which is surrounded by the isolating Cs^+ ions [Fig. 2(e)]. In contrast, $Cs_3Cu_2Cl_5$ includes the basic $[Cu_2Cl_5]$ structure and isolating Cs^+ ions, which is similar to $Cs_3Cu_2I_5$. The $[Cu_2Cl_5]$ consists of a $[CuCl_4]$ tetrahedron and a $[CuCl_3]$ planar triangle [35–37]. The tetrahedron and triangle are edge-shared to form the $[Cu_2Cl_5]$ structure as shown in Fig. 2(f). The different sites of Cl in the tetrahedron and the triangle could lead to the change of binding energy of Cl element, which is in agreement with the XPS results.

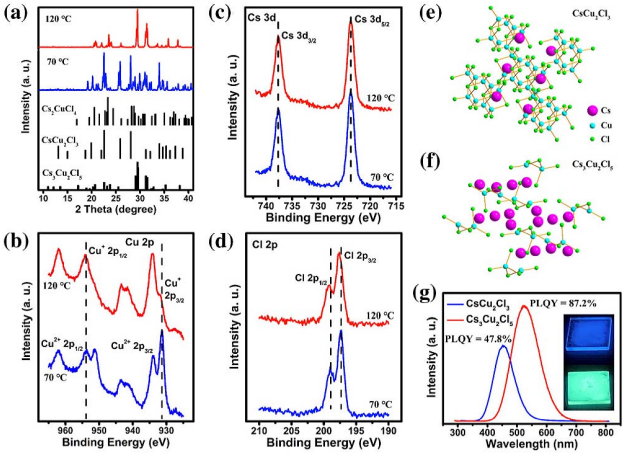

Fig. 2. (a) XRD patterns of the cesium copper chlorine colloidal perovskite synthesized at 70°C and 120°C, as well as the standard XRD patterns. High-resolution X-ray photoelectron spectroscopy (XPS) spectrum of (b) Cu 2p, (c) Cs 3d, (d) Cl 2p. (e), (f) Crystal structure of 3D $CsCu_2Cl_3$ and 0D $Cs_3Cu_2Cl_5$ NCs, respectively. The pink, bluish, and light-green balls represent the Cs, Cu, and Cl, respectively. (g) Photoluminescence spectra of chlorine colloidal perovskite synthesized at 70°C ($CsCu_2Cl_3$) and 120°C ($Cs_3Cu_2Cl_5$). The inset shows the luminescent photographs of $CsCu_2Cl_3$ (top) and $Cs_3Cu_2Cl_5$ (bottom) films excited under 254 nm UV light.

The PL spectra of $CsCu_2Cl_3$ and $Cs_3Cu_2Cl_5$ are shown in Fig. 2(g) with an emission centered at 453 and 518 nm for $CsCu_2Cl_3$ and $Cs_3Cu_2Cl_5$ NCs, respectively. The photographs of both samples excited under 254 nm UV light are presented in the inset of Fig. 2(g). The $CsCu_2Cl_3$ and $Cs_3Cu_2Cl_5$ NCs can emit bright-blue and green light, corresponding to a high PLQY value of 47.8% and 87.2%, respectively. In addition, they have broad emission spectra, which are evaluated by a high full width at half-maximum (FWHM) of ~100 nm. The high PLQY and broad emission of the inorganic lead-free cesium copper halide may originate from the copper halide clusters, leading to a greater charge localization and stronger excitonic effects [38].

To better understand the origin of the novel optical performance, photoluminescence exciton (PLE) spectra of $CsCu_2Cl_3$ and $Cs_3Cu_2Cl_5$ NCs were studied, as shown in Figs. 3(a) and 3(b). It is found that the more intense PLE fitted peaks of $CsCu_2Cl_3$ and $Cs_3Cu_2Cl_5$ NCs are at 301 and 297 nm, respectively. The PLE peaks at shorter wavelengths for both samples correspond to the energy states of the free carrier. The energy between dominant and minor peaks is considered the exciton binding energy (E_{eb}), which can be calculated using the following equation:

$$E_{eb} = E_{fc} - E_{es}, \quad (1)$$

where E_{fc} and E_{es} represent the energy of the free carrier and the excited state, respectively. In this work, the E_{eb} of $CsCu_2Cl_3$ and $Cs_3Cu_2Cl_5$ NCs are found to be ~320 and 500 meV, respectively. The strong exciton binding energy demonstrates that the location of the excited free carriers is around the Cu^+ ions [32]. In addition, the large Stokes shifts, which are regarded as the difference between absorption and emission spectra, are observed for both $CsCu_2Cl_3$ and $Cs_3Cu_2Cl_5$.

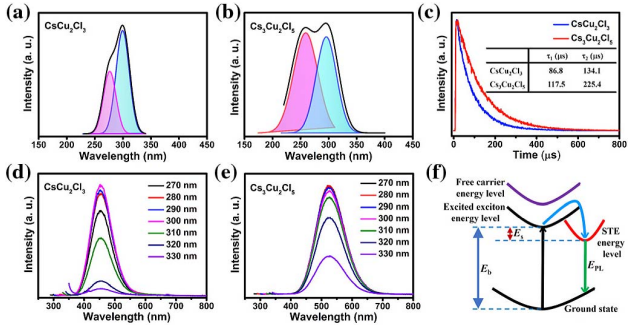

Fig. 3. Photoluminescence exciton (PLE) spectra of (a) $CsCu_2Cl_3$ and (b) $Cs_3Cu_2Cl_5$. (c) Room-temperature PL decay curves of 0D $Cs_3Cu_2Cl_5$ and 3D $CsCu_2Cl_3$ NCs. PL spectra of (d) $CsCu_2Cl_3$ and (e) $Cs_3Cu_2Cl_5$ NCs excited under different excitation wavelength. (f) Energy level schematic diagram of excited cesium copper chlorine nanocrystals.

To further study the mechanism of the exciton recombination in 0D $Cs_3Cu_2Cl_5$ and 3D $CsCu_2Cl_3$ NCs, the decay and exciting-wavelength dependence of PL for the both samples are investigated. Figure 3(c) shows the characterization results of photoluminescent decay curves, demonstrating the τ_1/τ_2 time of 117.5/225.4 and 86.8/134.1 μs for $Cs_3Cu_2Cl_5$ and $CsCu_2Cl_3$, respectively. Compared with the cesium lead halide ($CsPbX_3$, X = Cl, Br, I) perovskite nanocrystals, the lead-free as-prepared 0D $Cs_3Cu_2Cl_5$ and 3D $CsCu_2Cl_3$ NCs show a longer photoluminescent decay time, which might be due to the nonradiative recombination process caused by the self-trapped exciton (STE) effects [39]. Similar to the other low-dimension lead-free perovskite, such as $Cs_3Sb_2Br_9$ and $Cs_3Cu_2I_5$, the 0D $Cs_3Cu_2Cl_5$ and 3D $CsCu_2Cl_3$ NCs exhibit excellent optical properties, including a high PLQY, a broadband emission, and a large Stokes shift, which result from the presence of the STE effect. Besides, according to the previous works, the reduced dimensions of lead-free perovskite can lead to strong exciton localization, resulting in the increase of exciton binding energy. This is in good agreement with the calculation results for exciton binding energy of 3D $CsCu_2Cl_3$ (~320 meV) and 0D $Cs_3Cu_2Cl_5$ NCs (~500 meV). It has been reported that the STE effect may also account for the enhancement of exciton localization, as well as the FWHM in lead-free low-dimension perovskite. Therefore, the unique optical performance of our lead-free perovskite can be determined to originate from the STE effect.

The STE effect can be investigated by recording the PL spectra of the 0D $Cs_3Cu_2Cl_5$ and 3D $CsCu_2Cl_3$ NCs excited under different wavelengths as shown in Figs. 3(d) and 3(e), respectively. Negligible changes of PL emission peaks for both samples are found when excited under different wavelengths, indicating that the radiative recombination of 0D $Cs_3Cu_2Cl_5$ and 3D $CsCu_2Cl_3$ NCs is determined by an invariable emissive energy level. Considering the large Stokes shift of both samples, the invariable emissive energy level is associated with the presence of STE energy level. The formation of STE energy level is due to the excited-state structure induced by the Jahn–Teller distortion [40]. When cesium copper chlorine absorbs photons, the excited electrons may occupy the excited states and localize around the Cu^+ ions. Thus, the structure of the $[CuCl_4]$ tetrahedron may change because of the introduced inner stress. As a result, upon photoexcitation, the soft lattices of $Cs_3Cu_2Cl_5$ and $CsCu_2Cl_3$ can dissipate a large portion of strain energy, resulting in the distortion of their lattices, which is called Jahn–Teller distortion. The Jahn–Teller distortion induced from the $[CuCl_4]$ tetrahedron can further configure the electronic structure, possibly changing the original Cu^+ $3d^{10}$ to Cu^{2+} $3d^9$. Such localization of electrons and configuration of Cu^{2+} $3d^9$ are considered the reason for the formation of STE energy level [41]. Figure 3(f) shows the energy level diagram of the excited cesium copper chlorine. For PL with the STE effect, the emission energy is determined to be

$$E_{PL} = E_b - E_s, \tag{2}$$

where E_{PL} represents the PL emission energy, and E_b and E_s are the energy of the band gap and STE of the excited cesium copper chlorine NCs, respectively. Therefore, the Stokes shift can be explained as the energy loss induced by the formation of self-trapped excitons [42]. In addition, the high PLQY, long PL decay time, and broadband emission can be attributed to the direct emission of excitons from the STE level to the ground states, the energy transfer of excitons between excited states and the STE, and exciton–phonon coupling in the excited states, respectively [43].

Figure 4 shows the luminescent spectra and CIE chromaticity diagrams of $CsCu_2Cl_3$ and $Cs_3Cu_2Cl_5$ solid films upon 290 nm UV light excitation, which can be considered blue and green LEDs. The luminescence of $CsCu_2Cl_3$ and $Cs_3Cu_2Cl_5$ solid films exhibits broadband emission, which is consistent with the corresponding PL. Moreover, their CIE coordinates are located at (0.166, 0.214) and (0.274, 0.491), respectively, resulting from the broad emission with the FWHM of >100 nm. The high PLQY and broadband emission of $Cs_3Cu_2Cl_5$ and $CsCu_2Cl_3$ NCs with green and blue emission can facilitate solid-state lighting applications. Therefore, UV-pumped white light-emitting diodes (WLEDs) were fabricated using the $Cs_3Cu_2Cl_5$ and $CsCu_2Cl_3$ NCs as the green and blue components. To fabricate such WLEDs, red-emission $CaAlSiN_3:Eu^{2+}$ phosphors were first coated on a 290 nm commercial UV chip, and the PMMA blend of $Cs_3Cu_2Cl_5$ and $CsCu_2Cl_3$ NCs with an optimum ratio was coated on the top. Figure 5(a) exhibits the PL spectra of our WLEDs under driving voltages. With the increase of the driving voltages, the luminescent intensity of the WLEDs increases, suggesting that the emission of WLEDs can be regulated by the driving voltage. The photographs of the as-fabricated WLEDs in daylight and the operating WLEDs in dark are shown in the inset of Fig. 5(a), in which bright white light can be observed. In addition, the WLEDs exhibit an excellent white emission with a CIE color coordinate of (0.337, 0.338) [Fig. 5(b)], a color rendering index (CRI) of 94, and a correlated color

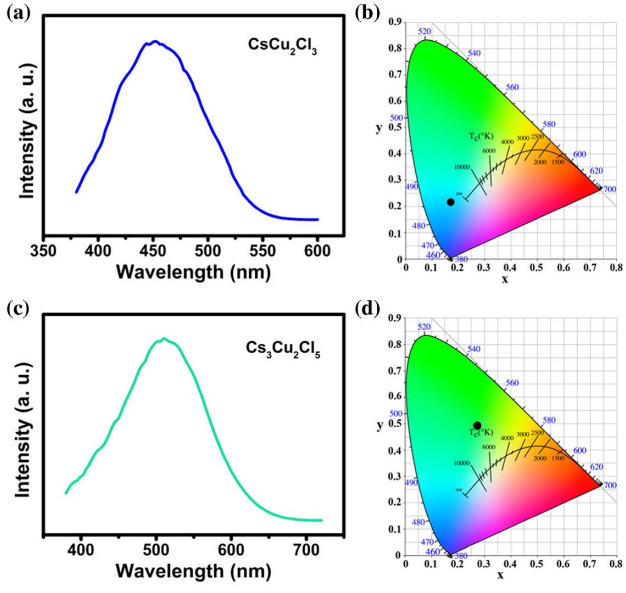

Fig. 4. (a), (c) Luminescent spectrum and (b), (d) CIE chromaticity diagram of $CsCu_2Cl_3$ and $Cs_3Cu_2Cl_5$ films excited on a 290 nm UV chip.

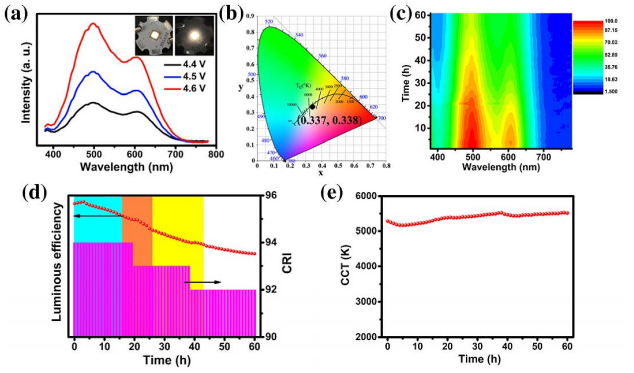

Fig. 5. (a) EL spectra of as-fabricated white light-emitting diodes (WLEDs). The insets are the photographs of the emissive WLEDs obtained in the daylight (left) and dark (right). (b) CIE chromaticity diagram of the WLEDs. (c) Pseudocolor plot of the EL spectra of long-time operating WLEDs. (d) Evolution of the normalized luminous efficiency (LE) and CRI values as functions of operating time. (e) CCT of the WLED as a function of the operating time in atmosphere.

temperature (CCT) of 5285 K, indicating the promising potential in solid-state lighting [44,45].

Furthermore, the operating stability of the WLEDs was investigated under a continuous driving voltage of 4.7 V. Figure 5(c) exhibits that the electroluminescence (EL) spectral intensity of the WLEDs reduces during the aging test. No shift is found for the EL peaks induced from $Cs_3Cu_2Cl_5$ NCs (green), $CsCu_2Cl_3$ NCs (blue), and $CaAlSiN_3:Eu^{2+}$ phosphors (red). Moreover, Fig. 5(d) shows that the luminous efficiency (LE) maintains 64% of its initial value even after 60 h in atmosphere (30°C and 50% RH). The appropriate and stable CCT (<6000) demonstrates the feasible performance of our WLEDs in long-time practical applications [Fig. 5(e)] [46]. The high CRI (>92) is also sustained after 60 h continuous operation as shown in Fig. 5(d). The performance attenuation of the WLEDs is attributed to the decrease of PL efficiency for cesium copper halide and phosphors under humidity in the air and rising temperature induced by long-time working of the UV chip. However, it is found that the attenuation of the WLEDs trends to change slightly after the aging test of 60 h, implying the excellent operating stability in atmosphere for hundreds of hours. Therefore, we believe that the highly efficient, stable, and nontoxic WLEDs can play a critical role in the next-generation lighting applications.

4. CONCLUSION

We have synthesized all-inorganic lead-free 0D $Cs_3Cu_2Cl_5$ and 3D $CsCu_2Cl_3$ NCs at 120°C and 70°C, respectively, indicating that the reaction temperature can determine the final component of cesium copper (monovalence) chlorine colloidal perovskite. Owing to the self-trapped exciton (STE) effect, the green-emission $Cs_3Cu_2Cl_5$ and blue-emission $CsCu_2Cl_3$ exhibit high PLQY, broadband emission, large Stokes shift, and long PL decay time. Such an STE effect can be attributed to the Jahn–Teller distortion induced by the $[CuCl_4]$ tetrahedron of $Cs_3Cu_2Cl_5$ and $CsCu_2Cl_3$. The highly efficient $Cs_3Cu_2Cl_5$ NCs can be used for the fabrication of the WLEDs, showing an excellent and stable performance with a high CRI and a moderate CCT even under long-time operation (60 h). The work therefore demonstrates the promising potential of nontoxic cesium copper chlorine perovskite and promotes the development of the novel solid-state lighting.

Funding. National Natural Science Foundation of China (61904023, 11974063); Postdoctoral Science Foundation of China (2019M653336); Natural Science Foundation of Chongqing (cstc2019jcyj-bshX0078); Innovation Program of Postdoctoral Program of Chongqing (CQBX201803).

Disclosures. The authors declare no conflicts of interest.

†These authors contributed equally to this paper.

REFERENCES

1. J. Shamsi, A. S. Urban, M. Imran, L. De Trizio, and L. Manna, "Metal halide perovskite nanocrystals: synthesis, post-synthesis modifications, and their optical properties," Chem. Rev. **119**, 3296–3348 (2019).
2. Q. A. Akkerman, G. Raino, M. V. Kovalenko, and L. Manna, "Genesis, challenges and opportunities for colloidal lead halide perovskite nanocrystals," Nat. Mater. **17**, 394–405 (2018).
3. X. Li, F. Cao, D. Yu, J. Chen, Z. Sun, Y. Shen, Y. Zhu, L. Wang, Y. Wei, Y. Wu, and H. Zeng, "All inorganic halide perovskites nanosystem: synthesis, structural features, optical properties and optoelectronic applications," Small **13**, 1603996 (2017).
4. F. Liu, Y. Zhang, C. Ding, S. Kobayashi, T. Izuishi, N. Nakazawa, T. Toyoda, T. Ohta, S. Hayase, T. Minemoto, K. Yoshino, S. Dai, and Q. Shen, "Highly luminescent phase-stable $CsPbI_3$ perovskite quantum dots achieving near 100% absolute photoluminescence quantum yield," ACS Nano **11**, 10373–10383 (2017).
5. Q. Wang, X. Wang, Z. Yang, N. Zhou, Y. Deng, J. Zhao, X. Xiao, P. Rudd, A. Moran, Y. Yan, and J. Huang, "Efficient sky-blue perovskite light-emitting diodes via photoluminescence enhancement," Nat. Commun. **10**, 5633 (2019).
6. J. Song, J. Li, L. Xu, J. Li, F. Zhang, B. Han, Q. Shan, and H. Zeng, "Room-remperature triple-ligand surface engineering synergistically boosts ink stability, recombination dynamics, and charge injection toward EQE-11.6% perovskite QLEDs," Adv. Mater. **30**, 1800764 (2018).
7. Q. Zhao, A. Hazarika, X. Chen, S. P. Harvey, B. W. Larson, G. R. Teeter, J. Liu, T. Song, C. Xiao, L. Shaw, M. Zhang, G. Li, M. C. Beard, and J. M. Luther, "High efficiency perovskite quantum dot solar cells with charge separating heterostructure," Nat. Commun. **10**, 2842 (2019).
8. L. M. Wheeler, E. M. Sanehira, A. R. Marshall, P. Schulz, M. Suri, N. C. Anderson, J. A. Christians, D. Nordlund, D. Sokaras, T. Kroll, S. P. Harvey, J. J. Berry, L. Y. Lin, and J. M. Luther, "Targeted ligand-exchange chemistry on cesium lead halide perovskite quantum dots for high-efficiency photovoltaics," J. Am. Chem. Soc. **140**, 10504–10513 (2018).
9. K. Chen, Q. Zhong, W. Chen, B. Sang, Y. Wang, T. Yang, Y. Liu, Y. Zhang, and H. Zhang, "Short-chain ligand-passivated stable α-$CsPbI_3$ quantum dot for all-inorganic perovskite solar cells," Adv. Funct. Mater. **29**, 1900991 (2019).
10. A. Swarnkar, A. R. Marshall, E. M. Sanehira, B. D. Chernomordik, D. T. Moore, J. A. Christians, T. Chakrabarti, and J. M. Luther, "Quantum dot-induced phase stabilization of α-$CsPbI_3$ perovskite for high-efficiency photovoltaics," Science **354**, 92–95 (2016).
11. J. Liu, B. Shabbir, C. Wang, T. Wan, Q. Ou, P. Yu, A. Tadich, X. Jiao, D. Chu, D. Qi, D. Li, R. Kan, Y. Huang, Y. Dong, J. Jasieniak, Y. Zhang, and Q. Bao, "Flexible, printable soft-X-ray detectors based on all-inorganic perovskite quantum dots," Adv. Mater. **31**, 1901644 (2019).

12. G. C. Adhikari, S. Thapa, H. Zhu, and P. Zhu, "Mg^{2+}-alloyed all-inorganic halide perovskites for white light-emitting diodes by 3D-printing method," Adv. Opt. Mater. **7**, 1900916 (2019).
13. S. Thapa, G. C. Adhikari, H. Zhu, A. Grigoriev, and P. Zhu, "Zn-alloyed all-inorganic halide perovskite-based white light-emitting diodes with superior color quality," Sci. Rep. **9**, 18636 (2019).
14. Z. Tan, J. Li, C. Zhang, Z. Li, Q. Hu, Z. Xiao, T. Kamiya, H. Hosono, G. Niu, E. Lifshitz, Y. Cheng, and J. Tang, "Highly efficient blue-emitting bi-doped Cs_2SnCl_6 perovskite variant: photoluminescence induced by impurity doping," Adv. Funct. Mater. **28**, 1801131 (2018).
15. J. Zhang, Y. Yang, H. Deng, U. Farooq, X. Yang, J. Khan, J. Tang, and H. Song, "High quantum yield blue emission from lead-free inorganic antimony halide perovskite colloidal quantum dots," ACS Nano **11**, 9294–9302 (2017).
16. M. Leng, Y. Yang, K. Zeng, Z. Chen, Z. Tan, S. Li, J. Li, B. Xu, D. Li, M. P. Hautzinger, Y. Fu, T. Zhai, L. Xu, G. Niu, S. Jin, and J. Tang, "All-Inorganic bismuth-based perovskite quantum dots with bright blue photoluminescence and excellent stability," Adv. Funct. Mater. **28**, 1704446 (2018).
17. F. Locardi, M. Cirignano, D. Baranov, Z. Dang, M. Prato, F. Drago, M. Ferretti, V. Pinchetti, M. Fanciulli, S. Brovelli, L. De Trizio, and L. Manna, "Colloidal synthesis of double perovskite $Cs_2AgInCl_6$ and Mn-doped $Cs_2AgInCl_6$ nanocrystals," J. Am. Chem. Soc. **140**, 12989–12995 (2018).
18. B. Yang, J. Chen, S. Yang, F. Hong, L. Sun, P. Han, T. Pullerits, W. Deng, and K. Han, "Lead-free silver-bismuth halide double perovskite nanocrystals," Angew. Chem. Int. Ed. **57**, 5359–5363 (2018).
19. Z. X. Zhang, C. Li, Y. Lu, X. W. Tong, F. X. Liang, X. Y. Zhao, D. Wu, C. Xie, and L. B. Luo, "Sensitive deep ultraviolet photodetector and image sensor composed of inorganic lead-free $Cs_3Cu_2I_5$ perovskite with wide bandgap," J. Phys. Chem. Lett. **10**, 5343–5350 (2019).
20. X. Zhao, G. Niu, J. Zhu, B. Yang, J. H. Yuan, S. Li, W. Gao, Q. Hu, L. Yin, K. H. Xue, E. Lifshitz, X. Miao, and J. Tang, "All-inorganic copper halide as a stable and self-absorption-free X-ray scintillator," J. Phys. Chem. Lett. **11**, 1873–1880 (2020).
21. H. Zhou, X. Liu, G. He, L. Fan, S. Shi, J. Wei, W. Xu, C. Yuan, N. Chai, B. Chen, Y. Zhang, X. Zhang, J. Zhao, X. Wei, J. Yin, and D. Tian, "Synthesis, crystal structure, UV-Vis adsorption properties, photoelectric behavior, and DFT computational study of all-inorganic and lead-free copper halide salt $K_2Cu_2Cl_6$," ACS Omega **3**, 14021–14026 (2018).
22. T. C. Jellicoe, J. M. Richter, H. F. Glass, M. Tabachnyk, R. Brady, S. E. Dutton, A. Rao, R. H. Friend, D. Credgington, N. C. Greenham, and M. L. Bohm, "Synthesis and optical properties of lead-free cesium tin halide perovskite nanocrystals," J. Am. Chem. Soc. **138**, 2941–2944 (2016).
23. Z. Luo, Q. Li, L. Zhang, X. Wu, L. Tan, C. Zou, Y. Liu, and Z. Quan, "0D $Cs_3Cu_2X_5$ (X = I, Br, and Cl) nanocrystals: colloidal syntheses and optical properties," Small **16**, 1905226 (2019).
24. R. Lin, Q. Guo, Q. Zhu, Y. Zhu, W. Zheng, and F. Huang, "All-inorganic $CsCu_2I_3$ single crystal with high-PLQY (≈ 15.7%) intrinsic white-light emission via strongly localized 1D excitonic recombination," Adv. Mater. **31**, 1905079 (2019).
25. T. Jun, K. Sim, S. Iimura, M. Sasase, H. Kamioka, J. Kim, and H. Hosono, "Lead-free highly efficient blue-emitting $Cs_3Cu_2I_5$ with 0D electronic structure," Adv. Mater. **30**, 1804547 (2018).
26. Z. Xiao, K. Du, W. Meng, D. B. Mitzi, and Y. Yan, "Chemical origin of the stability difference between copper(I)- and silver(I)-based halide double perovskite," Angew. Chem. Int. Ed. **129**, 12275–12279 (2017).
27. M. H. Du, "Emission trend of multiple self-trapped excitons in luminescent 1D copper halides," ACS Energy Lett. **5**, 464–469 (2020).
28. R. Roccanova, A. Yangui, G. Seo, T. D. Creason, Y. Wu, D. Y. Kim, M. H. Du, and B. Saparov, "Bright luminescence from nontoxic $CsCu_2X_3$ (X = Cl, Br, I)," ACS Mater. Lett. **1**, 459–465 (2019).
29. R. Roccanova, A. Yangui, H. Nhalil, H. Shi, M.-H. Du, and B. Saparov, "Near-unity photoluminescence quantum yield in blue-emitting $Cs_3Cu_2Br_{5-x}I_x (0 \le x \le 5)$," ACS Appl. Electron. Mater. **1**, 269–274 (2019).
30. T. Li, X. Mo, C. Peng, Q. Lu, C. Qi, X. Tao, Y. Ouyang, and Y. Zhou, "Distinct green electroluminescence from lead-free $CsCuBr_2$ halide micro-crosses," Chem. Commun. **55**, 4554–4557 (2019).
31. P. Yang, G. Liu, B. Liu, X. Liu, Y. Lou, J. Chen, and Y. Zhao, "All-inorganic Cs_2CuX_4 (X = Cl, Br, and Br/I) perovskite quantum dots with blue-green luminescence," Chem. Commun. **54**, 11638–11641 (2018).
32. P. Cheng, L. Sun, L. Feng, S. Yang, Y. Yang, D. Zheng, Y. Zhao, Y. Sang, R. Zhang, D. Wei, W. Deng, and K. Han, "Colloidal synthesis and optical properties of all-inorganic low-dimensional cesium halide nanocrystals," Angew. Chem. Int. Ed. **58**, 16087–16091 (2019).
33. P. Sebastia-Luna, J. Navarro-Alapont, M. Sessolo, F. Palazon, and H. J. Bolink, "Solvent-free synthesis and thin-film deposition of cesium copper halides with bright blue photoluminescence," Chem. Mater. **31**, 10205–10210 (2019).
34. L. Xie, B. Chen, F. Zhang, Z. Zhao, X. Wang, L. Shi, Y. Liu, L. Huang, R. Liu, B. Zou, and Y. Wang, "Highly luminescent and stable lead-free cesium copper halide perovskite powders for UV-pumped phosphor-converted light-emitting diodes," Photon. Res. **8**, 768–775 (2020).
35. C. Brink, N. F. Binnendijk, and J. van de Linde, "The crystal structures of $CsCu_2Cl_3$ and $CsAg_2I_3$," Acta Crystallogr. **7**, 176 (1953).
36. S. Hull and P. Berastegui, "Crystal structures and ionic conductivities of ternary derivatives of the silver and copper monohalides-II: ordered phases within the $(AgX)_x$-$(MX)_{1-x}$ and $(CuX)_x$-$(MX)_{1-x}$ (M = K, Rb and Cs; X = Cl, Br and I) systems," J. Solid State Chem. **177**, 3156–3173 (2004).
37. T. A. Malakhovskaya-Rosokha, I. E. Barchii, A. I. Pogodin, A. P. Kokhan, I. P. Stercho, and E. Y. Peresh, "Interaction of components in the RbI-CsI-CuI quasi-ternary system," Russian J. Inorg. Chem. **58**, 577–580 (2013).
38. L. Lian, M. Zheng, W. Zhang, L. Yin, X. Du, P. Zhang, X. Zhang, J. Gao, D. Zhang, L. Gao, G. Niu, H. Song, R. Chen, X. Lan, J. Tang, and J. Zhang, "Efficient and reabsorption-free radioluminescence in $Cs_3Cu_2I_5$ nanocrystals with self-trapped excitons," Adv. Sci. **7**, 2000195 (2020).
39. X. Huang, Q. Sun, and B. Devakumar, "Facile low-temperature solid-state synthesis of efficient blue-emitting $Cs_3Cu_2I_5$ powder phosphors for solid-state lighting," Mater. Today Chem. **17**, 100288 (2020).
40. L. Wang, Z. Shi, Z. Ma, D. Yang, F. Zhang, X. Ji, M. Wang, X. Chen, G. Na, S. Chen, D. Wu, Y. Zhang, X. Li, L. Zhang, and C. Shan, "Colloidal synthesis of ternary copper halide nanocrystals for high-efficiency deep-blue light-emitting diodes with a half-lifetime above 100 h," Nano Lett. **20**, 3568–3576 (2020).
41. Z. Ma, Z. Shi, C. Qin, M. Cui, D. Yang, X. Wang, L. Wang, X. Ji, X. Chen, J. Sun, D. Wu, Y. Zhang, X. J. Li, L. Zhang, and C. Shan, "Stable yellow light-emitting devices based on ternary copper halides with broadband emissive self-trapped excitons," ACS Nano **14**, 4475–4486 (2020).
42. S. Li, J. Luo, J. Liu, and J. Tang, "Self-trapped excitons in all-inorganic halide perovskites: fundamentals, status, and potential applications," J. Phys. Chem. Lett. **10**, 1999–2007 (2019).
43. K. M. McCall, C. C. Stoumpos, S. S. Kostina, M. G. Kanatzidis, and B. W. Wessels, "Strong electron–phonon coupling and self-trapped excitons in the defect halide perovskites $A_3M_2I_9$ (A = Cs, Rb; M = Bi, Sb)," Chem. Mater. **29**, 4129–4145 (2017).
44. G. C. Adhikari, S. Thapa, H. Zhu, A. Grigoriev, and P. Zhu, "Synthesis of $CsPbBr_3$ and transformation into Cs_4PbBr_6 crystals for white light emission with high CRI and tunable CCT," J. Phys. Chem. C **123**, 12023–12028 (2019).
45. G. C. Adhikari, P. A. Vargas, H. Zhu, A. Grigoriev, and P. Zhu, "Tetradic phosphor white light with variable CCT and superlative CRI through organolead halide perovskite nanocrystals," Nanoscale Adv. **1**, 1791–1798 (2019).
46. P. Du, L. Luo, and W. Cheng, "Neoteric Mn^{2+}-activated $Cs_3Cu_2I_5$ dazzling yellow-emitting phosphors for white-LED," J. Am. Ceram. Soc. **103**, 1149–1155 (2019).